CONDENSED MATTER PHYSICS

The electronic thickness of graphene

Peter Rickhaus[1]*, Ming-Hao Liu[2]*, Marcin Kurpas[3], Annika Kurzmann[1], Yongjin Lee[1], Hiske Overweg[1,4], Marius Eich[1], Riccardo Pisoni[1], Takashi Taniguchi[5], Kenji Watanabe[5], Klaus Richter[6], Klaus Ensslin[1], Thomas Ihn[1]

When two dimensional crystals are atomically close, their finite thickness becomes relevant. Using transport measurements, we investigate the electrostatics of two graphene layers, twisted by θ = 22° such that the layers are decoupled by the huge momentum mismatch between the K and K′ points of the two layers. We observe a splitting of the zero-density lines of the two layers with increasing interlayer energy difference. This splitting is given by the ratio of single-layer quantum capacitance over interlayer capacitance C_m and is therefore suited to extract C_m. We explain the large observed value of C_m by considering the finite dielectric thickness d_g of each graphene layer and determine $d_g \approx 2.6$ Å. In a second experiment, we map out the entire density range with a Fabry-Pérot resonator. We can precisely measure the Fermi wavelength λ in each layer, showing that the layers are decoupled. Our findings are reproduced using tight-binding calculations.

INTRODUCTION

The van der Waals stacking technique allows scientists to bring two conductive crystalline layers into atomically close proximity (*1*). This has been exploited in a variety of experiments, including the formation of layer-polarized, counterpropagating Landau levels (*2*) and experiments that build on strong capacitive coupling such as Coulomb drag measurements (*3*) or interlayer exciton condensation (*4*, *5*).

There are two main approaches to bring two conductive layers in close proximity while suppressing an overlap of the layer wave functions: One approach introduces a thin layer of hexagonal boron nitride (hBN) [see, e.g., (*3*, *4*, *6*)] as depicted in Fig. 1 (A and B), and the other twists the layers by a large angle (θ > 5°) [see Fig. 1 (C and D)] (*2*, *7*–*9*). In the former case, decoupling is achieved by spatial separation. In the latter case, the layers are ultimately close, but they remain decoupled because of a large momentum mismatch ($\mathbf{K}_t - \mathbf{K}_b$) between the upper and lower layers (Fig. 1D). Experimental signatures of decoupling are an increased interlayer resistance (*10*, *11*) and layer-polarized Landau levels at large magnetic fields (*2*, *9*).

In this work, we perform quantum transport experiments to monitor precisely the coupling, coherence, and tunability of two graphene layers that are in close proximity to each other. In one device, we separate the two layers by a thin layer of hBN with thickness $d = 3.5$ nm (sample A), and in the other device, we twist the layers by 22° to decouple them (sample B).

In the first experiment, we observe a splitting of the charge neutrality points of the two layers in the parameter plane of top- and back-gate voltage (V_{tg} and V_{bg}). By analyzing the splitting, we extract a geometric capacitance C_m between the graphene layers. For sample A, we obtain the expected value given the thickness and dielectric constant of the intermediate hBN layer. However, for sample B, C_m is three times larger than the geometric capacitance between two ideal capacitor plates, separated by the interlayer distance between carbon atoms $d_{CC} = 3.4$ Å, assuming vacuum in between. We argue that, because of the finite electronic thickness of graphene, the plates of the capacitor are effectively closer than d_{CC}, leading to the enhanced C_m. We find good agreement with a capacitive model where we take the electronic thickness of graphene into account.

In the second experiment, on sample B, we use a gate-defined Fabry-Pérot cavity to monitor the layer densities, coherence, and interlayer coupling of wave functions. The cavities are formed by gate-defined p-n junctions, which act as semitransparent lateral "mirrors" of the interferometer (*12*–*16*). Either only one or both layers can be tuned to the bipolar p-n-p regime. In both layers, we observe the lowest energy Fabry-Pérot mode, corresponding to λ = 600 nm, while the wavelength in the other cavity can be shorter by a factor of 10. We model the observed interference pattern using tight-binding calculations, assuming completely decoupled layers. This second experiment confirms the assumed electronic decoupling and, for arbitrary gate voltages, the electrostatic model that considers thick graphene.

RESULTS

Zero-density lines

The numerical conductance dG/dV_{tg} as a function of V_{tg} and V_{bg} is shown in Fig. 2A for sample A and Fig. 2B for sample B. In both cases, two pronounced curved lines are observed, corresponding to a dip in the conductance G. The lines cross at zero gate voltages, and the splitting between these lines increases with increasing difference in V_{tg} and V_{bg}. One line (following the yellow dashed line) is affected more strongly by the top-gate voltage and therefore corresponds to the condition for charge neutrality in the upper graphene layer, whereas the other line (red dashed) indicates charge neutrality in the lower layer.

From electrostatic considerations, we find that the zero-density condition can be expressed as (details are given in the Supplementary Materials)

$$\left.\frac{\partial V_{tg}}{\partial V_{bg}}\right|_{n_b=0} \approx -\frac{C_{bg}}{C_{tg}}\left(1+\frac{C_{qt}}{C_m}\right)$$

$$\left.\frac{\partial V_{bg}}{\partial V_{tg}}\right|_{n_t=0} \approx -\frac{C_{tg}}{C_{bg}}\left(1+\frac{C_{qb}}{C_m}\right)$$

[1]Solid State Physics Laboratory, ETH Zürich, CH-8093 Zürich, Switzerland. [2]Department of Physics, National Cheng Kung University, Tainan 70101, Taiwan. [3]Institute of Physics, University of Silesia in Katowice, 41-500 Chorzów, Poland. [4]Microsoft Research Cambridge, Cambridge, UK. [5]National Institute for Materials Science, 1-1 Namiki, Tsukuba 305-0044, Japan. [6]Institute of Theoretical Physics, University of Regensburg, D-93040 Regensburg, Germany.
*Corresponding author. Email: peterri@phys.ethz.ch (P.R.); minghao.liu@phys.ncku.edu.tw (M.-H.L.)

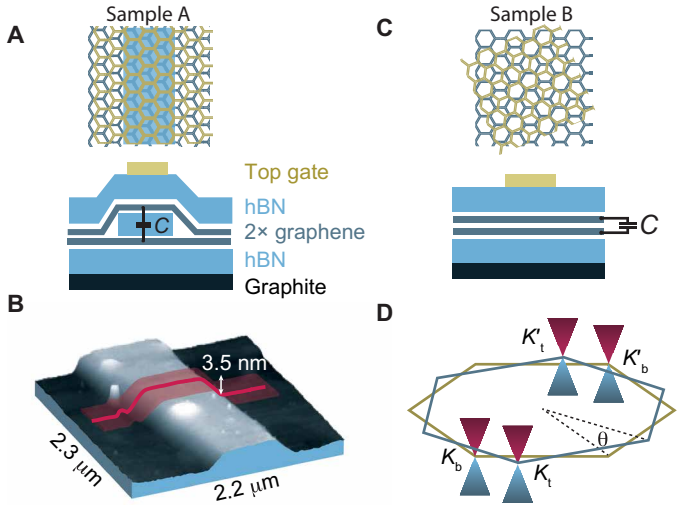

Fig. 1. Experimental design. (**A**) Top and side views of two aligned layers of graphene that are decoupled in the middle (blue part) by a thin intermediate layer of hBN. A graphite back gate and a local top gate allow controlling the density and, thereby, the carrier wavelength in the upper and lower layers individually. (**B**) Using atomic force microscopy (AFM), we measured the encapsulated hBN layer to be 3.5 nm thick (sample A). (**C**) Alternatively, the decoupling wave functions can be achieved by twisting two graphene layers (sample B). (**D**) For large twist angles, the valleys in the upper/lower layer ($\mathbf{K}_t$, $\mathbf{K}_b$) are separated by a large momentum, leading to an effective electronic decoupling of the layers.

where C_{bg} (C_{tg}) is the geometric capacitance of the bottom (top) graphene to the bottom (top) gate (see Fig. 2C) and the density in the bottom (top) graphene layer is n_b (n_t). The capacitance measured between the two graphene plates is C_m. The quantum capacitance $C_{qt} = e^2\mathcal{D}_t(\mathcal{E}_F)$ of the top layer is proportional to the density of states at the Fermi energy in the top layer (the analog relation holds for the bottom layer). For a single sheet of graphene, the slope of the zero-density line in a (V_{tg}, V_{bg}) map is given by the ratio $-C_{bg}/C_{tg}$ (prefactor in the above equations). For the two-layer system, the deviations from linearity of the constant-density line are governed by the ratio between quantum capacitance and C_m, respectively. Therefore, the splitting is smaller in sample B, where C_m is larger, as compared to sample A, where C_m is smaller.

Analytical formulas for the zero-density lines [i.e., $V_{bg}(V_{tg})\,|_{n_t=0}$ and $V_{bg}(V_{tg})\,|_{n_b=0}$] can be calculated using the ideal density of states of defect-free graphene and are depicted in Fig. 2 (A and B) for the different electrostatic configurations (i.e., with or without hBN between the graphene sheets). The formulas and details of the calculation are given in the Supplementary Materials. Fitting these curves to the data allows us to extract C_m, which is the only free fitting parameter. The other capacitances in the problem are given by the thickness of the top and bottom hBN, i.e., $C_{tg} = \epsilon_{hBN}/d_t$ with $\epsilon_{hBN} = 3.3\epsilon_0$. A discussion for the precision of this method is given in the Supplementary Materials.

For sample A, we obtain an interlayer capacitance of $C_m = 0.81\ \mu F\ cm^{-2}$, which corresponds to the expected value for a plate separation of $d = 3.5$ nm and the hBN dielectric constant of $\epsilon_{hBN} = 3.3\epsilon_0$. For sample B, we determine a large interlayer capacitance $C_m = 7.5 \pm 0.7\ \mu F\ cm^{-2}$. This value is three times larger than the capacitance between two thin plates, separated by vacuum and an interlayer distance of $d_{CC} = 3.4$ Å, which is the expected distance between two graphene layers (*17*, *18*). Consistent with our findings, large interlayer capacitance values have been reported in (*9*) in large perpendicular magnetic fields (quantum Hall regime) with a capacitance model that is only valid for $n_t = -n_b$. A detailed explanation for the large value of C_m has not been given so far.

The finite thickness of graphene

To understand the origin of such a large effective interlayer capacitance, we need to take into account the finite thickness of graphene, as this reduces the effective distance between the capacitor plates, leading to an enhanced interlayer capacitance. Therefore, we have estimated the extent of the p_z orbitals of carbon atoms in graphene from first-principles calculations (details are given in the Supplementary Materials). We calculated the integrated local density of states profile $\rho(z)$ of single-layer graphene in the energy range $E \in [-3, 3]$ eV from the charge neutrality point at $E_c = 0$ eV. In this energy range, the bands are of pure p_z orbital character without contributions from the s-, p_x- and p_y-like orbitals). The calculated integrated local density of states ILDOS(z) as a function of distance from the center of the carbon atom is shown in Fig. 2D. From the charge distribution, we then calculated the expectation value of the position operator $\langle z \rangle$ for one lobe of p_z orbital (positive z). The values are shown as black dashed lines in the figure. Since there is a substantial amount of charge at $|z| > \langle z \rangle$, we have to take into account the induced charge density $\Delta\rho = \rho(E = 0) - \rho(E)$ in an external electric field E, which determines the dielectric thickness of graphene (*19*), defined as the distance from the center of carbon atoms to the point at which the dielectric constant of graphene $\epsilon = 6.9\epsilon_0$ decays to the vacuum permittivity. The dielectric thickness is the relevant quantity if considering a single layer of graphene to be a nanocapacitor on its own. The dielectric thickness of graphene d_g is indicated by the blue shaded region in Fig. 2D, with values according to (*19*).

To check whether twisted bilayer graphene (tBLG) displays a qualitatively different electrostatic behavior than AA- and AB-stacked BLGs, we performed first-principles calculations of tBLG with a twist angle of 22° (details of computations are given in the Supplementary Materials). In Fig. 2E, we show the comparison of the induced charge density $\Delta\rho(z) := \rho(0) - \rho(E_z)$ for tBLG, AA BLG, and AB BLG under an external electric field $E_z = 1$ V/nm perpendicular to the BLG lattice. The interlayer distance of AA and AB BLGs was set to 3.51 Å to fit the average distance between tBLG layers. Nevertheless, the results are representative and insensitive to small deviations of interlayer distance from the optimized value or to the choice of the dispersive correction due to van der Waals forces (see the Supplementary Materials). One can see that the responses of the different BLGs to the external electric field E_z are almost the same on the outer side of the BLG, while they are very different in the interlayer region. For $z = 13 \pm 0.7$ Å, we observe a flattening of $\Delta\rho(z)$ in the case of tBLG compared to AA and AB BLGs. Within this region, the amplitude of $\Delta\rho(z)$ for tBLG is 15 times smaller than for AB BLG and 50 times smaller for AA BLG, demonstrating a qualitatively different electrostatic picture.

These calculations motivate a simplified capacitance model where the measured capacitance C_m (between the center of charge of each layer) contains two dielectric materials coupled in series: graphene with $\epsilon_g = 6.9\epsilon_0$ (*19*) and thickness d_g and an interlayer region of vacuum with thickness $d_{inter} = d_{CC} - d_g$ and a dielectric constant of vacuum. Therefore, $1/C_m = d_g/\epsilon_g + (d_{CC} - d_g)/\epsilon_0$. With $d_{CC} = 3.4$ Å and the measured capacitance, we determine a dielectric thickness

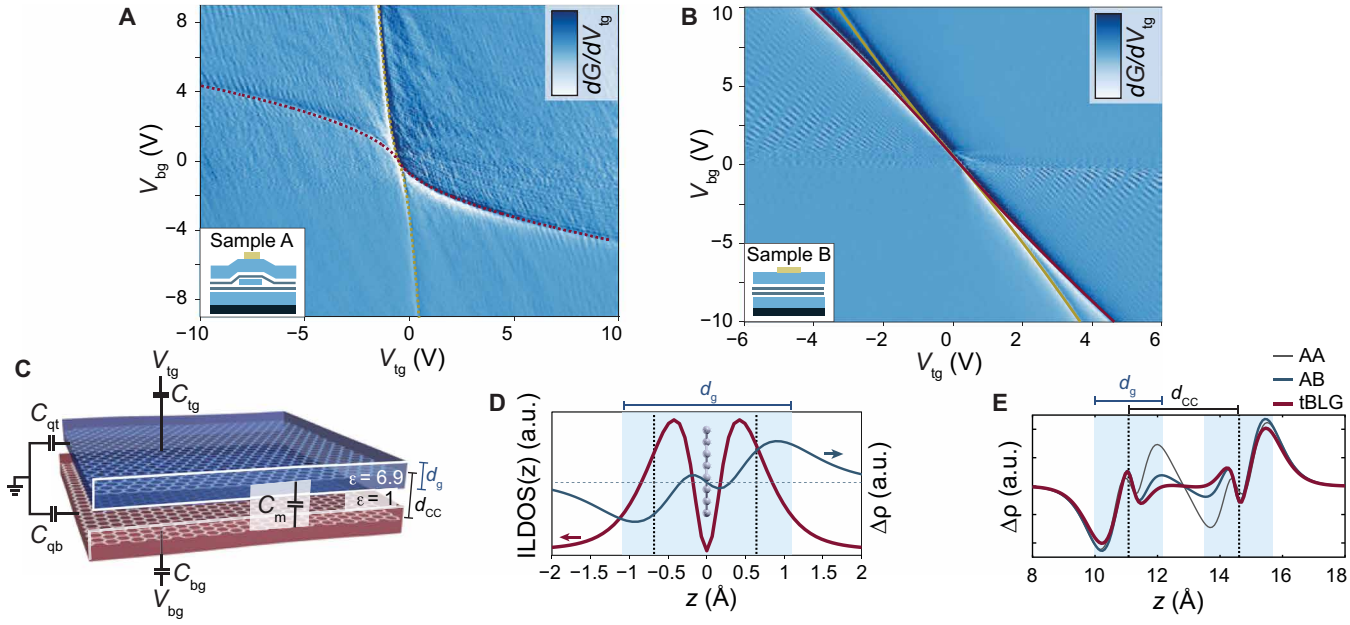

Fig. 2. Zero-density lines. Numerical derivative of the two-terminal conductance $dG/dV_{tg}(V_{tg}, V_{bg})$ for a device where the graphene layers are (**A**) separated by a thin hBN layer (sample A) or (**B**) in atomic vicinity but twisted by a large angle (sample B). Zero-density lines in the upper (yellow) and lower (red) graphene layers are obtained from numerical calculations. (**C**) Schematic electrostatic configuration of sample B. (**D**) Calculated integrated local density of states ILDOS(z) of p_z-like orbital of carbon atoms in graphene (red) and the induced charge density $\Delta\rho(z) = \rho(0) - \rho(E_z)$ per carbon atom under an external electric field E_z. The geometry of graphene is shown on the background picture. The graphene sheet is placed at $z = 0$ and extends in the xy plane. Positions of black dotted lines mark the effective thickness of graphene calculated from the expectation value of the position operator $\langle z \rangle = 0.66$ Å. The blue shaded region shows the dielectric thickness of graphene extracted from the dielectric permittivity (*19*). (**E**) Comparison of $\Delta\rho(z)$ for bilayer graphene (BLG) in AA stacking configuration (gray line), AB Bernal (blue line), and twisted BLG (tBLG) (red line). The position of graphene layers is marked by vertical dashed lines, and the blue shaded regions depict the dielectric thickness of single-layer graphene. a.u., arbitrary units.

of $d_g = 2.6 \pm 0.2$ Å from our measurements, which is in agreement with theoretical predictions in single-layer graphene exhibiting 2.4 Å (*19*). Using a similar model for the hBN device with $1/C_m = d_g/\epsilon_g + d_{hBN}/\epsilon_{hBN}$, we find $d_{hBN} = 35$ Å, which is in excellent agreement with the thickness measured with the atomic force microscopy (AFM). However, the correction by the thickness of graphene (≈1 Å) in this case is of the order of the measurement accuracy of our AFM.

Our analysis is generally valid in the large angle regime (>5°). If the twist gets reduced, then the bands of the upper and lower layers start to hybridize at smaller energies, leading to a reduction of Fermi velocity and an increase of quantum capacitance. We expect to observe a stronger splitting in this case. For small twists, once the layers are coupled at low enough energies, there will be only one line in the gate-gate map at zero total density. Regarding the interlayer capacitance, in Fig. 2E, one can see that the interlayer charge distribution is different for AA-stacked graphene and tBLG. This indicates a modification of the interlayer capacitance toward smaller angles.

Decoupled Fabry-Pérot interferences

In the next step, we use a Fabry-Pérot interferometer to measure the layer density of sample B for arbitrary gate voltages and compare the results to tight-binding simulations based on an elaborate electrostatic model. The analysis of the Fabry-Pérot resonance pattern will allow us to determine the Fermi wavelength in the individual layers and will reveal that the graphene layers are indeed electronically decoupled. In Fig. 3 (A and B), we show dG/dV_{tg} for top gates, sized $L = 190$ and 320 nm, respectively. For both cases, the cavity width $W \gg L$. The zero-density lines are depicted in yellow for the top layer and dark red for the bottom layer.

The Fabry-Pérot resonator exhibits a pattern that can be qualitatively understood by considering the layer densities in the regions underneath and outside the top gate, as depicted in Fig. 3C. The density in the single-gated outer regions is affected only by V_{bg}. Since $V_{bg} < 0$, the outer regions are p-doped (blue colored). For small voltages, labeled (1) and (2) in Fig. 3 (A and C), the density of each of the two layers is comparable, i.e., there is only a small energy difference U between the two layers (see Fig. 3D). A p-n-p cavity below the top gate is formed for a sufficiently positive top-gate voltage (2) in both layers. Given a large energy difference between the layers, it becomes possible to create a p-n-p cavity in only one layer (3) or also in both (4).

As soon as a p-n-p cavity is formed, the conductance is modulated by standing waves, leading to the observed resonance pattern in Fig. 3 (A and B). In the inner region (3), only one set of Fabry-Pérot resonances, related to zero density in the upper layer, is observed. For densities beyond the zero-density line of the lower layer (dark red line in Fig. 3A), a more complex resonance pattern appears.

The resonance pattern is determined by the Fabry-Pérot condition, where the jth resonance is $j = 2L/\lambda_F = k_F L/\pi$, where L is the cavity size and λ_F is the Fermi wavelength. Note that $k_F = \sqrt{\pi n}$ is given by the density in the top and bottom layer. As expected, we observe a finer spacing of the resonance pattern for the larger cavity (Fig. 3B with $L = 320$ nm) as compared to the smaller cavity (Fig. 3A with $L = 190$ nm). In the region between the zero-density lines, 6 resonances are observed at large U for $L = 190$ nm and even 10 resonances for $L = 320$ nm, i.e., it is possible to fill 10 modes in the upper resonator while there is still no cavity formed in the lower layer. By assuming that L is given by the lithographic size, it follows

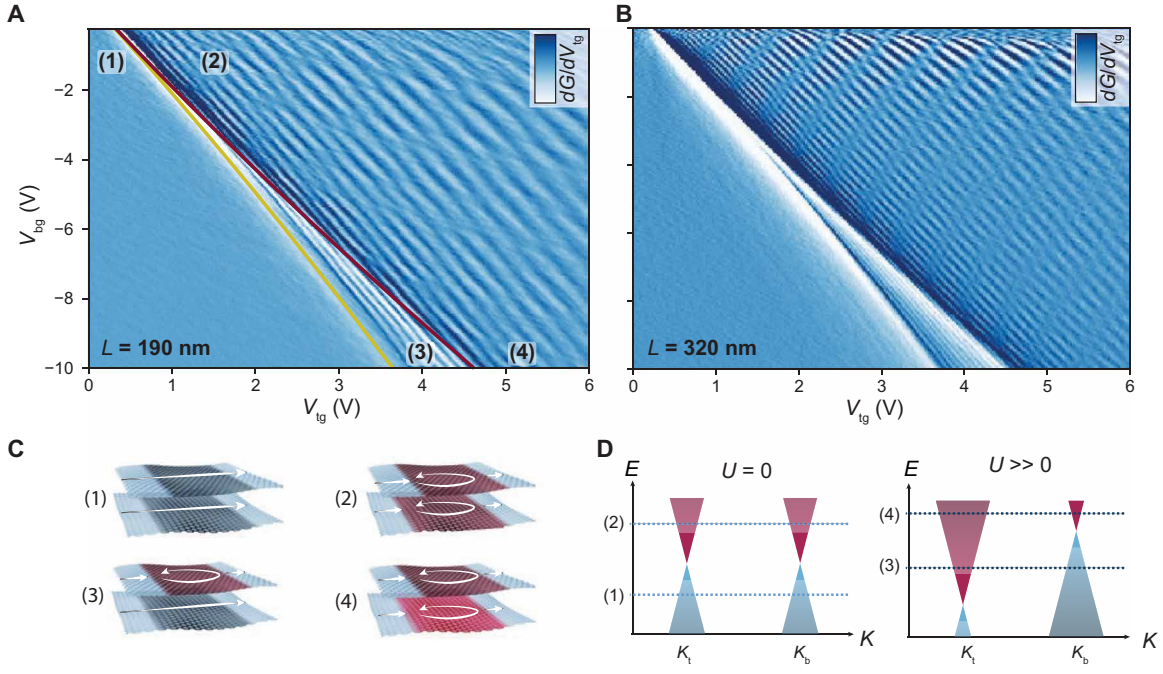

Fig. 3. Fabry-Pérot interference pattern. Differential conductance $dG/dV_{tg}(V_{tg}, V_{bg})$ for gates of length (**A**) L = 190 nm and (**B**) L = 320 nm for sample B. (**C**) Sketches of the local density in the two Fabry-Pérot layers. Blue regions are p-doped, and red regions are n-doped. The sketches (1) to (4) show different gating configurations, marked correspondingly in (A). (**D**) As the difference in gate voltages increases, the energies in the top and bottom layers will shift by the interlayer energy difference U.

that $\lambda_{F,\,bottom}$ = 640 nm and $\lambda_{F,\,top}$ = 64 nm once the first mode fits into the cavity in the bottom layer at large U. Therefore, the wavelength can differ by an order of magnitude between two graphene layers despite the fact that those layers are atomically close.

In the measurement, especially for the larger cavity (Fig. 3B), it can also be seen that the oscillation amplitude is largest for either small values of V_{bg} or close to the zero-density lines. Under these conditions, either the graphene part tuned only by V_{bg} or the cavity below the top gate is close to zero density; therefore, the density profile along the junction is especially flat, leading to a smooth transition between the cavity and the outer region. The enhanced oscillation amplitude can be understood by considering that smooth p-n interfaces act as strong angular filters (*13*, *15*).

Simulation of density and transport

We now compare the resonance pattern to tight-binding simulations. The underlying density profiles $n_t(x)$ and $n_b(x)$ are obtained from a self-consistent electrostatic model where we assume that the dispersion relation remains linear, such that the carrier density formulas (*20*) derived for single-layer graphene with quantum capacitance (*21*, *22*) taken into account can be readily applied. The extremely thin spacing between the two graphene layers leads to a notable electrostatic coupling. Effectively, the channel potential of the top layer plays the role as a gate for the bottom layer and vice versa. For the twisted bilayer sample B (see Fig. 4A), the electrostatic coupling between the layers is significant, as can be seen by comparing to the classical density profiles (dashed lines). In Fig. 4B, we calculate the interlayer energy difference $U(V_{tg}, V_{bg})$ for sample B. The maximum value that we can reach is U = 80 meV in our device. We note here that the formula given in (*2*, *9*) for the displacement field [i.e., $D = 1/2(C_{tg}V_{tg} - C_{bg}V_{bg})$] only holds under the condition $n_t = -n_b$. Apparently, lines of constant U (white lines in Fig. 4B) do not have a constant slope in the (V_{tg}, V_{bg}) map. A more detailed comparison is given in the Supplementary Materials.

To see whether the electrostatic model is in agreement with the experiment, we perform transport simulations based on a real-space Green's function approach, considering two dual-gated, electronically decoupled graphene layers. To optimize the visibility of the Fabry-Pérot interference fringes, we implement periodic boundary hoppings along the transverse dimension (*23*), equivalent to the assumption of infinitely wide graphene samples. This is justified since $W \gg L$ in our device. The normalized conductances $g_t(V_{tg}, V_{bg})$ and $g_b(V_{tg}, V_{bg})$ for the top and bottom graphene layers, respectively, are calculated using carrier density profiles $n_t(x)$ and $n_b(x)$. The numerical derivative of the results is shown in Fig. 4C. To compare with the measurement, we consider the numerical derivative $\partial g_{tot}/\partial V_{tg}$ of the sum $g_t + g_b = g_{tot}$ (Fig. 4D). The excellent agreement to the measurement (Fig. 3B) is a strong indication that the wave functions of the top and bottom layers are essentially decoupled and individually tunable.

The tight-binding theory allows us to compare the electrostatic model to the experiment and to estimate the precision of the obtained value for the graphene interlayer capacitance C_m. For the cavity L = 320 nm and for V_{bg} = −10 V, we observe $N = 11 \pm 1$ modes between the two zero-density lines in the experimental data (Fig. 3B) and $N = 11 \pm 0.5$ modes in the tight-binding data (Fig. 4D). Since the splitting of zero-density lines is proportional to C_m, we estimate the error to be ≈10% for C_m, and therefore, we estimate the dielectric thickness of graphene $d_g = 2.6 \pm 0.2$ Å.

DISCUSSION

We have performed transport experiments for two representative cases of decoupled layers of graphene. We investigated two devices: one where decoupling is achieved by a thin hBN layer (sample A)

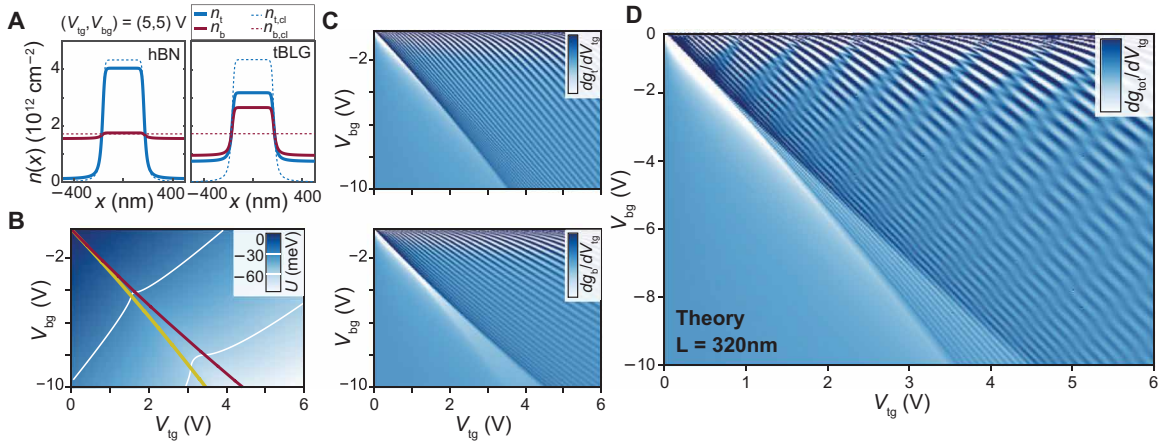

Fig. 4. Simulations. (**A**) Numerically calculated layer density profiles $n_t(x)$ (blue) and $n_b(x)$ (red), shaped by a top gate with a size of 320 nm and a global back gate for sample A with an hBN spacer (left) and for sample B with a large-angle tBLG (right). The depicted gating condition is (V_{tg}, V_{bg}) = (5,5) V. The dashed lines show the classical result (neglecting the quantum capacitance). (**B**) Interlayer energy difference $U(V_{tg}, V_{bg})$. Zero-density lines are marked with yellow and red lines. (**C**) Numerical derivative of the calculated normalized conductance, $\partial g/\partial V_{tg}$. Using the obtained n_t and n_b, the conductance $g(V_{tg}, V_{bg})$ of the top layer (top) and the bottom layer (bottom) are calculated individually using a real-space Green's function approach. (**D**) The sum of the two differential conductances $\partial g_{tot}/\partial V_{tg}$ reproduces the experimental data in Fig. 3B.

and the other where the decoupling is given by the large momentum mismatch between graphene layers due to a large twist angle (sample B). In both cases, we observed a clear splitting of the charge neutrality points in a two-terminal measurement with the strength of the splitting given by C_q/C_m. By comparing to a self-consistent electrostatic model, we extracted a very large geometric interlayer capacitance $C_m = 7.5 \pm 0.7\ \mu F\ cm^{-2}$ for the tBLG sample, which we explained by taking into account an effective dielectric thickness of graphene of $d_g = 2.6 \pm 0.2$ Å. In a further step, we investigated Fabry-Pérot fringes that originate from p-n-p cavities created with a local top gate and a global back gate. We were able to form a p-n-p cavity in only one of the layers and could tune the wavelength in each layer individually. In an $L = 320$ nm cavity, we observed the first mode in the bottom layer, while we had already filled 10 modes in the top layer. The measurements are in very good agreement with the results from tight-binding simulations based on two graphene layers electronically decoupled but electrostatically coupled through their quantum capacitances. Our work emphasizes that the finite thickness of two-dimensional materials is relevant for the electronic properties of van der Waals heterostructures where conducting layers are in close proximity.

MATERIALS AND METHODS

To achieve ballistic transport, we encapsulate (*24*) either tBLG (sample B) or graphene–3.5-nm hBN–graphene between hBN layers (sample A) and use a graphite bottom gate (*25*, *26*). The alignment of the graphene layers is controlled by the method described in (*27*, *28*), and we used twist angles (between the graphene layers) $\theta \approx 0°$ for sample A and $\theta \approx 22°$ for sample B. The thickness of the top, bottom, and intermediate hBN layers is determined by AFM. Electrical one-dimensional contacts are achieved by reactive ion etching and evaporation of Cr/Au. Top gates of sizes 320 and 190 nm are defined by electron beam lithography. By adjusting the top-gate voltage V_{tg} and the back-gate voltage V_{bg}, a Fabry-Pérot cavity can be formed below the top gate. Two-terminal linear conductance measurements are performed using a low-frequency lock-in technique (177 Hz) at the temperature $T = 1.5$ K.

SUPPLEMENTARY MATERIALS

Supplementary material for this article is available at http://advances.sciencemag.org/cgi/content/full/6/11/eaay8409/DC1

Fig. S1. Measurement on two further devices.
Fig. S2. Accuracy of the fitting procedure.
Fig. S3. Interlayer energy difference U.
Fig. S4. Induced density profile for AA and AB bilayer graphene.
Fig. S5. Schematics of the crystalline structure of the unit cell of 22° tBLG with 196 carbon atoms.
Fig. S6. Comparison of the induced charge density $\Delta\rho(z)$ for AA and AB bilayer graphene.
Fig. S7. Schematic model for gated, decoupled BLG.
Table S1. Calculated interlayer distances for AA and AB BLGs for different types of dispersion corrections.
References (*29*–*38*)

REFERENCES AND NOTES

1. K. S. Novoselov, A. Mishchenko, A. Carvalho, A. H. Castro Neto, 2D materials and van der Waals heterostructures. *Science* **353**, aac9439 (2016).
2. J. D. Sanchez-Yamagishi, J. Y. Luo, A. F. Young, B. M. Hunt, K. Watanabe, T. Taniguchi, R. C. Ashoori, P. Jarillo-Herrero, Helical edge states and fractional quantum Hall effect in a graphene electron-hole bilayer. *Nat. Nanotechnol.* **12**, 118–122 (2017).
3. R. V. Gorbachev, A. K. Geim, M. I. Katsnelson, K. S. Novoselov, T. Tudorovskiy, I. V. Grigorieva, A. H. MacDonald, S. V. Morozov, K. Watanabe, T. Taniguchi, L. A. Ponomarenko, Strong Coulomb drag and broken symmetry in double-layer graphene. *Nat. Phys.* **8**, 896–901 (2012).
4. X. Liu, K. Watanabe, T. Taniguchi, B. I. Halperin, P. Kim, Quantum Hall drag of exciton condensate in graphene. *Nat. Phys.* **13**, 746–750 (2017).
5. X. Liu, Z. Hao, K. Watanabe, T. Taniguchi, B. I. Halperin, P. Kim, Interlayer fractional quantum Hall effect in a coupled graphene double-layer. *Nat. Phys.* **15**, 893–897 (2019).
6. M. T. Greenaway, E. E. Vdovin, A. Mishchenko, O. Makarovsky, A. Patanè, J. R. Wallbank, Y. Cao, A. V. Kretinin, M. J. Zhu, S. V. Morozov, V. I. Fal'ko, K. S. Novoselov, A. K. Geim, T. M. Fromhold, L. Eaves, Resonant tunnelling between the chiral Landau states of twisted graphene lattices. *Nat. Phys.* **11**, 1057–1062 (2015).
7. A. Luican, G. Li, A. Reina, J. Kong, R. R. Nair, K. S. Novoselov, A. K. Geim, E. Y. Andrei, Single-layer behavior and its breakdown in twisted graphene layers. *Phys. Rev. Lett.* **106**, 126802 (2011).
8. A. V. Rozhkov, A. O. Sboychakov, A. L. Rakhmanov, F. Nori, Electronic properties of graphene-based bilayer systems. *Phys. Rep.* **648**, 1–104 (2016).
9. J. D. Sanchez-Yamagishi, T. Taychatanapat, K. Watanabe, T. Taniguchi, A. Yacoby, P. Jarillo-Herrero, Screening, and layer-polarized insulating states in twisted bilayer graphene. *Phys. Rev. Lett.* **108**, 076601 (2012).
10. T. Chari, R. Ribeiro-Palau, C. R. Dean, K. Shepard, Resistivity of rotated graphite–graphene contacts. *Nano Lett.* **16**, 4477–4482 (2016).

11. R. Ribeiro-Palau, C. Zhang, K. Watanabe, T. Taniguchi, J. Hone, C. R. Dean, Twistable electronics with dynamically rotatable heterostructures. *Science* **361**, 690–693 (2018).
12. W. Liang, M. Bockrath, D. Bozovic, J. H. Hafner, M. Tinkham, H. Park, Fabry-Perot interference in a nanotube electron waveguide. *Nature* **411**, 665–669 (2001).
13. V. V. Cheianov, V. I. Fal'ko, Selective transmission of Dirac electrons and ballistic magnetoresistance of *n-p* junctions in graphene. *Phys. Rev. B* **74**, 041403 (2006).
14. A. F. Young, P. Kim, Quantum interference and Klein tunnelling in graphene heterojunctions. *Nat. Phys.* **5**, 222–226 (2009).
15. P. Rickhaus, R. Maurand, M.-H. Liu, M. Weiss, K. Richter, C. Schönenberger, Ballistic interferences in suspended graphene. *Nat. Commun.* **4**, 2342 (2013).
16. A. Varlet, M.-H. Liu, V. Krueckl, D. Bischoff, P. Simonet, K. Watanabe, T. Taniguchi, K. Richter, K. Ensslin, T. Ihn, Fabry-Pérot interference in gapped bilayer graphene with broken anti-klein tunneling. *Phys. Rev. Lett.* **113**, 116601 (2014).
17. Y. Huang, J. Wu, K. C. Hwang, Thickness of graphene and single-wall carbon nanotubes. *Phys. Rev. B* **74**, 245413 (2006).
18. S. J. Haigh, A. Gholinia, R. Jalil, S. Romani, L. Britnell, D. C. Elias, K. S. Novoselov, L. A. Ponomarenko, A. K. Geim, R. Gorbachev, Cross-sectional imaging of individual layers and buried interfaces of graphene-based heterostructures and superlattices. *Nat. Mater.* **11**, 764–767 (2012).
19. J. Fang, W. G. Vandenberghe, M. V. Fischetti, Microscopic dielectric permittivities of graphene nanoribbons and graphene. *Phys. Rev. B* **94**, 45318 (2016).
20. M.-H. Liu, Theory of carrier density in multigated doped graphene sheets with quantum correction. *Phys. Rev. B* **87**, 125427 (2013).
21. S. Luryi, Quantum capacitance devices. *Appl. Phys. Lett.* **52**, 501–503 (1988).
22. T. Fang, A. Konar, H. Xing, D. Jena, Mobility in semiconducting graphene nanoribbons: Phonon, impurity, and edge roughness scattering. *Phys. Rev. B* **78**, 205403 (2008).
23. M.-H. Liu, K. Richter, Efficient quantum transport simulation for bulk graphene heterojunctions. *Phys. Rev. B* **86**, 115455 (2012).
24. L. Wang, I. Meric, P. Y. Huang, Q. Gao, Y. Gao, H. Tran, T. Taniguchi, K. Watanabe, L. M. Campos, D. A. Muller, J. Guo, P. Kim, J. Hone, K. L. Shepard, C. R. Dean, One-dimensional electrical contact to a two-dimensional material. *Science* **342**, 614–617 (2013).
25. A. A. Zibrov, C. Kometter, H. Zhou, E. M. Spanton, T. Taniguchi, K. Watanabe, M. P. Zaletel, A. F. Young, Tunable interacting composite fermion phases in a half-filled bilayer-graphene Landau level. *Nature* **549**, 360–364 (2017).
26. H. Overweg, H. Eggimann, X. Chen, S. Slizovskiy, M. Eich, R. Pisoni, Y. Lee, P. Rickhaus, K. Watanabe, T. Taniguchi, V. Fal'ko, T. Ihn, K. Ensslin, Electrostatically induced quantum point contacts in bilayer graphene. *Nano Lett.* **18**, 553–559 (2018).
27. K. Kim, M. Yankowitz, B. Fallahazad, S. Kang, H. C. P. Movva, S. Huang, S. Larentis, C. M. Corbet, T. Taniguchi, K. Watanabe, S. K. Banerjee, B. J. Le Roy, E. Tutuc, Van der Waals heterostructures with high accuracy rotational alignment. *Nano Lett.* **16**, 1989–1995 (2016).
28. K. Kim, A. DaSilva, S. Huang, B. Fallahazad, S. Larentis, T. Taniguchi, K. Watanabe, B. J. Le Roy, A. H. MacDonald, E. Tutuc, Tunable moiré bands and strong correlations in small-twist-angle bilayer graphene. *Proc. Natl. Acad. Sci. U.S.A.* **114**, 3364–3369 (2017).
29. H. Schmidt, T. Lüdtke, P. Barthold, E. M. Cann, V. I. Fal'ko, R. J. Haug, Tunable graphene system with two decoupled monolayers. *Appl. Phys. Lett.* **93**, 172108 (2008).
30. P. Giannozzi, S. Baroni, N. Bonini, M. Calandra, R. Car, C. Cavazzoni, D. Ceresoli, G. L. Chiarotti, M. Cococcioni, I. Dabo, A. D. Corso, S. Fabris, G. Fratesi, S. de Gironcoli, R. Gebauer, U. Gerstmann, C. Gougoussis, A. Kokalj, M. Lazzeri, L. Martin-Samos, N. Marzari, F. Mauri, R. Mazzarello, S. Paolini, A. Pasquarello, L. Paulatto, C. Sbraccia, S. Scandolo, G. Sclauzero, A. P. Seitsonen, A. Smogunov, P. Umari, R. M. Wentzcovitch, Quantum ESPRESSO: A modular and open-source software project for quantum simulations of materials. *J. Phys. Condens. Matter* **21**, 395502 (2009).
31. P. Giannozzi, O. Andreussi, T. Brumme, O. Bunau, M. B. Nardelli, M. Calandra, R. Car, C. Cavazzoni, D. Ceresoli, M. Cococcioni, N. Colonna, I. Carnimeo, A. D. Corso, S. de Gironcoli, P. Delugas, R. A. Di Stasio Jr., A. Ferretti, A. Floris, G. Fratesi, G. Fugallo, R. Gebauer, U. Gerstmann, F. Giustino, T. Gorni, J. Jia, M. Kawamura, H.-Y. Ko, A. Kokalj, E. Küçükbenli, M. Lazzeri, M. Marsili, N. Marzari, F. Mauri, N. L. Nguyen, H.-V. Nguyen, A. Otero-de-la-Roza, L. Paulatto, S. Poncé, D. Rocca, R. Sabatini, B. Santra, M. Schlipf, A. P. Seitsonen, A. Smogunov, I. Timrov, T. Thonhauser, P. Umari, N. Vast, X. Wu, S. Baroni, Advanced capabilities for materials modelling with Quantum ESPRESSO. *J. Phys. Condens. Matter* **29**, 465901 (2017).
32. A. M. Rappe, K. M. Rabe, E. Kaxiras, J. D. Joannopoulos, Optimized pseudopotentials. *Phys. Rev. B* **41**, 1227–1230 (1990).
33. J. P. Perdew, K. Burke, M. Ernzerhof, Generalized gradient approximation made simple. *Phys. Rev. Lett.* **77**, 3865–3868 (1996).
34. L. Bengtsson, Dipole correction for surface supercell calculations. *Phys. Rev. B* **59**, 12301–12304 (1999).
35. H. J. Monkhorst, J. D. Pack, Special points for Brillouin-zone integrations. *Phys. Rev. B* **13**, 5188–5192 (1976).
36. S. Grimme, J. Antony, S. Ehrlich, H. Krieg, A consistent and accurate ab initio parametrization of density functional dispersion correction (DFT-D) for the 94 elements H-Pu. *J. Chem. Phys.* **132**, 154104 (2010).
37. S. Grimme, Semiempirical GGA-type density functional constructed with a long-range dispersion correction. *J. Comput. Chem.* **27**, 1787–1799 (2006).
38. V. Barone, M. Casarin, D. Forrer, M. Pavone, M. Sambi, A. Vittadini, Role and effective treatment of dispersive forces in materials: Polyethylene and graphite crystals as test cases. *J. Comput. Chem.* **30**, 934–939 (2009).

Acknowledgments

Funding: We acknowledge financial support from the European Graphene Flagship, the Swiss National Science Foundation via NCCR Quantum Science and Technology, the Deutsche Forschungsgemeinschaft through SFB 1277 project A07, and the Taiwan Ministry of Science (107-2112-M-006-004-MY3 and 107-2627-E-006-001) and Ministry of Education (Higher Education Sprout Project). This work is also supported by the National Science Center under the contract DEC-2018/29/B/ST3/01892 and, in part, by PAAD Infrastructure cofinanced by Operational Programme Innovative Economy, Objective 2.3. Growth of hBN crystals was supported by the Elemental Strategy Initiative conducted by MEXT, Japan and the CREST (JPMJCR15F3), JST. **Author contributions:** P.R. fabricated the device and performed measurements and data analysis. Tight-binding calculations and density simulations were provided by M.H.-L. Density functional theory calculations were performed by M.K. A.K., Y.L., H.O., M.E., and R.P. were involved in the fabrication and measurements. T.T. and K.W. provided hBN crystals. K.R., K.E., and T.I. supervised the work. All authors contributed to the manuscript. **Competing interests:** The authors declare that they have no competing interests. **Data and materials availability:** All data needed to evaluate the conclusions in the paper are present in the paper and/or the Supplementary Materials. Additional data related to this paper may be requested from the authors.

Submitted 23 July 2019
Accepted 16 December 2019
Published 13 March 2020
10.1126/sciadv.aay8409

Citation: P. Rickhaus, M.-H. Liu, M. Kurpas, A. Kurzmann, Y. Lee, H. Overweg, M. Eich, R. Pisoni, T. Taniguchi, K. Watanabe, K. Richter, K. Ensslin, T. Ihn, The electronic thickness of graphene. *Sci. Adv.* **6**, eaay8409 (2020).

Science Advances

The electronic thickness of graphene

Peter Rickhaus, Ming-Hao Liu, Marcin Kurpas, Annika Kurzmann, Yongjin Lee, Hiske Overweg, Marius Eich, Riccardo Pisoni, Takashi Taniguchi, Kenji Watanabe, Klaus Richter, Klaus Ensslin and Thomas Ihn

Sci Adv **6** (11), eaay8409.
DOI: 10.1126/sciadv.aay8409